Journal of
Synchrotron
Radiation

ISSN 0909-0495

Received 18 January 2012
Accepted 1 March 2012

Implementation of a beam deflection system for studies of liquid interfaces on beamline I07 at Diamond

Thomas Arnold,* Chris Nicklin, Jonathan Rawle, John Sutter, Trevor Bates, Brian Nutter, Gary McIntyre and Martin Burt

Diamond Light Source, Harwell Science and Innovation Campus, Chilton, Didcot OX11 0DE, UK. E-mail: tom.arnold@diamond.ac.uk

X-ray optics, based on a double-crystal deflection scheme, that enable reflectivity measurements from liquid surfaces/interfaces have been designed, built and commissioned on beamline I07 at Diamond Light Source. This system is able to deflect the beam onto a fixed sample position located at the centre of a five-circle diffractometer. Thus the incident angle can be easily varied without moving the sample, and the reflected beam is tracked either by a moving Pilatus 100K detector mounted on the diffractometer arm or by a stationary Pilatus 2M detector positioned appropriately for small-angle scattering. Thus the system can easily combine measurements of the reflectivity from liquid interfaces ($Q_z >$ 1 Å^{-1}) with off-specular data collection, both in the form of grazing-incidence small-angle X-ray scattering (GISAXS) or wider-angle grazing-incidence X-ray diffraction (GIXD). The device allows operation over the energy range 10–28 keV.

Keywords: X-ray reflectivity; GIXD; GISAXS; air–water; liquid–liquid.

1. Introduction

The use of X-ray reflectivity to study the structure of interfaces is well established. However, studies of liquid interfaces present a particular problem at synchrotron sources because neither the surface nor the synchrotron can be tilted to achieve the variation of incident angle required. There are several ways around this problem and most of these are explained in some detail by Daillant (2000). In short, for monochromatic X-rays the beam must be deflected onto the sample. Historically this has been done either by X-ray mirrors or by Bragg reflection from a single crystal. In both cases the sample and detector move to track the deflected beam. The mechanics of this is specialized and generally requires a dedicated beam deflection stage and a purpose-built sample stage and diffractometer (for example, see Smilgies *et al.*, 2005; Schlossman *et al.*, 1997).

An alternative arrangement of optics for achieving this deflection without the need to move the sample position was first implemented on beamline ID15 at ESRF (Honkimäki *et al.*, 2006). The system uses sequential Bragg reflections from silicon crystals, Si(111) and Si(220), to produce an overall deflection of the beam. This geometry means that the sample no longer has to track the deflected beam since, as the crystals are rotated, the beam pivots at a fixed sample position.

Here we have extended this concept to design a system (hereafter referred to as the 'double-crystal deflector' or DCD) that is energy tunable over the energy range 10–28 keV (significantly lower energy than ID15) and has been incorporated into the existing beamline I07 at Diamond Light Source. This is a new design that accounts for the particular requirements of the beamline space constraints and therefore has a different approach to a similar system 'LISA' recently constructed on beamline P08 at PETRA III (Seeck *et al.*, 2012; Murphy *et al.*, 2010).

The particular advantage of this design for beamline I07 is that it fits well with the existing equipment and means that full advantage can be taken of the diffractometer and the P2M detector, which can quickly and conveniently be used for grazing-incidence X-ray diffraction (GIXD) and grazing-incidence small-angle X-ray scattering (GISAXS) in combination with the reflectivity measurements.

The design of beamline I07 will be published in detail elsewhere. Of particular relevance here is the vertical scattering geometry of the double-crystal monochromator which uses silicon (111) crystals and a beam size at the sample position of ~150 µm (v) × 200 µm (h). We will discuss the relevance of these features in more detail below.

2. DCD design overview

The concept of using two crystals to achieve the required sample deflection is explained by Honkimäki *et al.* (2006). In short, the beam is deflected in a way that is analogous to a

standard double-crystal monochromator, first by ⟨111⟩ but then back in the opposite direction by ⟨220⟩. This produces an overall beam deflection, $2\Delta\theta$, where $\Delta\theta$ is equal to the difference in the Bragg angles of these two lattice planes. Both crystals are mounted on the same rotation stage that has its axis well aligned with the incoming beam. By rotating the crystal pair around this axis the beam path can be moved so that the angle of incidence at a fixed sample position is varied. The vertical incidence angle, α, is given by

$$\sin\alpha = \sin\varphi \sin 2\Delta\theta, \tag{1}$$

where φ is the angle of rotation about the incoming beam axis (full range available is $-15^\circ \leq \varphi \leq 90^\circ$). When $\varphi = 90^\circ$ (scattering in the vertical plane), α is at its maximum value of $2\Delta\theta$ and this corresponds to a maximum possible momentum transfer for a reflectivity measurement of greater than 2.54 Å^{-1} for all energies. If required, the system can also go to negative angles which correspond to angles approaching the sample from below the horizontal.

The change in φ also results in a change in the horizontal deflection, β, defining the angles that the detector must follow to track the beam,

$$\sin\beta = \cos\varphi \sin 2\Delta\theta. \tag{2}$$

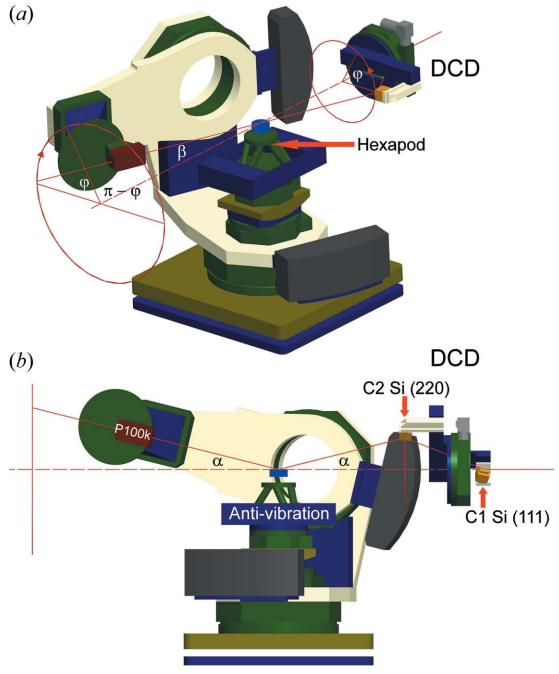

Figure 1
Two projections of the arrangement of the DCD and diffractometer showing some of the angles discussed in the text. (*a*) This projection shows the DCD scattering in the horizontal plane ($Q_z = 0$). The vertical incident angle is varied by rotating the DCD angle φ. The sample is mounted on a hexapod located in the centre of the diffractometer, which then tracks the deflected beam as φ is varied. The angle β is the beam deflection in the horizontal plane. (*b*) Side projection showing the DCD with $\varphi = 45^\circ$, to illustrate the beam deflection in the vertical plane α. In both of these plots the DCD is shown with the maximum radius of rotation corresponding to the minimum X-ray energy. A change in energy is achieved by reducing this radius by moving C2 towards the centre.

Figs. 1 and 2 show a schematic of the arrangement of the DCD within the beamline, giving an overview of the scattering geometry. In contrast to ID15, which operates at much higher energy, on I07 the crystals are arranged in Bragg rather than Laue geometry. To achieve the ability to vary the energy, the second crystal is mounted on a linear stage that is itself mounted on the main circle. This means that the position of the second crystal can be varied to intercept the beam as the deflection angle from the first crystal varies with wavelength. The whole system is located within a pre-existing beamline and as such there were some space limitations that constrained to the optical design.

It is notable that a change in wavelength also results in a small change in the distance of the sample position from the second crystal. This can be compensated for by allowing the

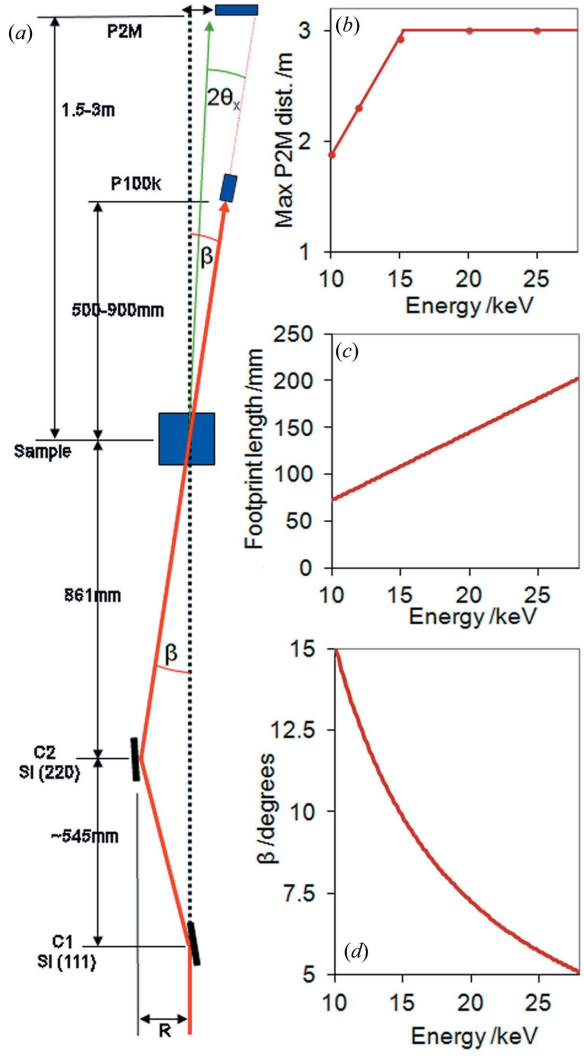

Figure 2
(*a*) Plan view schematic representation of the arrangement of the DCD crystals, diffractometer and another larger detector (P2M) upstream of the diffractometer that can also move to cover the deflected beam. (*b*) The maximum distance achievable for the P2M detector that will still allow the deflected beam to hit the detector. (*c*) The variation with X-ray energy of the footprint size (150 µm beam) at the sample position for Q_z = 0.021 Å^{-1} (the critical edge of water). (*d*) The maximum horizontal deflection β as a function of energy.

beam to traverse the face of the second crystal slightly, effectively changing the crystal separation along the beam direction (C1–C2, see Fig. 2) and keeping the C2–sample distance fixed (along the beam direction). The effective crystal separation (C1–C2) varies by ±1 mm over the whole energy range, which is a small movement relative to the overall length of the crystals (45 mm).

Good alignment of the axis of the rotation stage to the incident beam is essential for good performance. To achieve this alignment, pitch and yaw adjustments of the whole DCD are included in the design, which, in combination with small changes in the mirror deflection angles, can align the system without the need for translational adjustments. Each crystal has both pitch (to allow the Bragg condition to be met) and roll adjustment (to steer the beam). The first crystal is mounted on a short radial stage so that it can be accurately positioned at the centre of rotation of the main circle, and also allowing C1 to be retracted when the DCD is not in use, enabling the X-ray beam to bypass the DCD optics. An additional linear stage is mounted back to back with the C2 radial stage, allowing some simple diagnostics to be positioned behind C2 for the purposes of alignment scans and as an incident beam monitor.

The whole system is enclosed within a vacuum vessel (best observed vacuum 2×10^{-8} mbar) in order to improve the transmission and reduce the air scattering, particularly for the softer X-rays in the usable range. Importantly for the other uses of the beamline, this arrangement also allows for a vacuum beam path when the DCD is not in use. When in use, a large beryllium window mounted on a nose-cone is used to cover the full range of exit angles. The vacuum vessel is mounted on a support frame that is isolated from the internal optics *via* bellows. The internal optics are mounted on legs which are attached to a large granite block in order to reduce transmitted vibrations. This granite block is arranged so that it allows the diffractometer counterweights to pass underneath the vacuum vessel.

The DCD is positioned upstream of the main 2+3 geometry diffractometer (Huber) on which the sample is mounted. This geometry decouples the detector arms from the sample manipulation. The sample stage is mounted on a hexapod (Micos) which provides height adjustment and any other alignment required. This sits on an active anti-vibration system (Halcyonics) which isolates the sample from any minor vibrations produced by the moving detector arm. The principal diffractometer mounted detector for reflectivity and GIXD measurements is a Dectris Pilatus 100K. If required for GISAXS or otherwise, a Dectris Pilatus 2M detector is mounted further downstream on a movable stage that can be positioned to detect the deflected beam and thereby remove the need for the detector arm movement.

There are a number of sample environment options supplied by the beamline and the flexibility to mount a wide range of user-supplied equipment within certain space constraints defined by the precise experimental set-up. These include Langmuir troughs (Nima) of various sizes [including 200 × 400 mm, 200 × 100 mm, a small volume insert (30–50 cc) and other small troughs] and a controlled atmosphere enclosure. A sample changer and humidity control are also in development. In most cases the use of a large sample environment enclosure means that there is less space for the inclusion of an ion chamber or fast shutter *etc*. Typically there is about 50 cm of space along the beamline to incorporate the sample environments and any other diagnostics/apparatus required.

2.1. Intensity variation and elliptical polarization

The geometry of the beamline optics has a considerable influence on the intensity of the incident beam at the sample position. In particular, the flux transmitted through the DCD depends on the rotation angle φ, relative to the monochromator. This arises from two factors.

The first is the dependence of the Bragg reflectivity on the polarization of the incident beam. The intensity of a diffracted X-ray beam (*e.g.* from a crystal reflection with a Bragg angle θ_B) is dependent upon whether or not the beam is polarized in the diffracting plane. The structure factor for a beam that is polarized in the diffracting plane (π) is less than for a beam polarized perpendicular to the diffracting plane (σ). The ratio of the structure factors is $\cos 2\theta_B$. According to the dynamical diffraction theory that applies to perfect crystals, the Darwin width for a π-polarized beam is proportionately reduced and the loss owing to photoelectric absorption is increased (Zachariasen, 1945). Because the X-ray beam produced by the I07 undulator is almost entirely horizontally polarized, the electric field incident on the DCD can be decomposed into its σ- and π-components when the DCD is rotated by the angle φ about the incident beam,

$$E_\sigma = E_0 \sin\varphi, \qquad E_\pi = E_0 \cos\varphi. \tag{3}$$

Thus, at arbitrary φ both components of the polarization must be considered. If the complex reflectivity of the Bragg reflection at a given incidence angle, $\theta \simeq \theta_B$, is $R_\sigma(\theta)$ for the σ-component and $R_\pi(\theta)$ for the π-component, then the total electric field of the diffracted beam for a plane wave incident at the angle θ will be

$$E'_\sigma = R_\sigma(\theta) E_0 \sin\varphi, \qquad E'_\pi = R_\pi(\theta) E_0 \cos\varphi. \tag{4}$$

Notice that, because $R_\pi(\theta) < R_\sigma(\theta)$, the total diffracted intensity will be less at $\varphi = 0^\circ$ than at $\varphi = 90^\circ$. For the same reason, at intermediate values of φ the DCD will change the polarization of the beam. Both effects will be strongest if $\theta_B = 45^\circ$, for which $R_\pi(\theta) \simeq 0$. Although, for the crystal reflections used here, $\theta_B < 45^\circ$ for most X-ray energies, this polarization effect is greatest for soft X-rays simply because $\theta_B \to 45^\circ$. In addition, a small phase difference between the complex reflectivity of σ and π polarizations gives the beam emerging from the DCD a slightly elliptical polarization. However, this beam remains to a very high degree polarized parallel to the liquid sample's surface. Even at $\varphi = 45^\circ$, where the ellipticity is strongest, only a few percent of the intensity is polarized normal to the sample's surface, and this can be neglected.

The second reason for the variation of DCD throughput is that the monochromator–DCD system selects different ranges

of X-ray wavelengths and directions as φ is varied. This can best be understood by expanding the concept of the DuMond diagram (DuMond, 1937). The classic DuMond diagram results from Bragg's Law ($2d \sin\theta = \lambda$) and is a plot of wavelength, λ, *versus* incidence angle, θ. It treats crystals constrained to diffract in the same plane, but this still permits consecutive crystals to be arranged either 'non-dispersively' (+−), in which one crystal deflects the beam clockwise and the other anticlockwise or *vice versa*, or 'dispersively' (++), in which they both deflect the beam either clockwise or anti-clockwise. The wavelengths and in-plane angles, θ, of the rays that are transmitted with significant intensity can be estimated by overlapping the plots for the different crystals on a single DuMond diagram. The non-dispersive configuration requires the traces of the two crystals to be directly superimposed, while the dispersive configuration requires the trace of the second crystal to be reflected about the λ-axis with respect to the trace of the first (Fig. 3). It is evident that the two configurations transmit very different ranges of wavelengths and angles if the incident beam divergence is larger than the Darwin width of the reflection. An analysis of the I07 DCD is more complex because the DCD crystals may be rotated relative to the upstream monochromator through a range of angles from $\varphi = -15^\circ$ to 90° (*i.e.* from below the horizontal to the vertical). In the case of I07 the monochromator and the

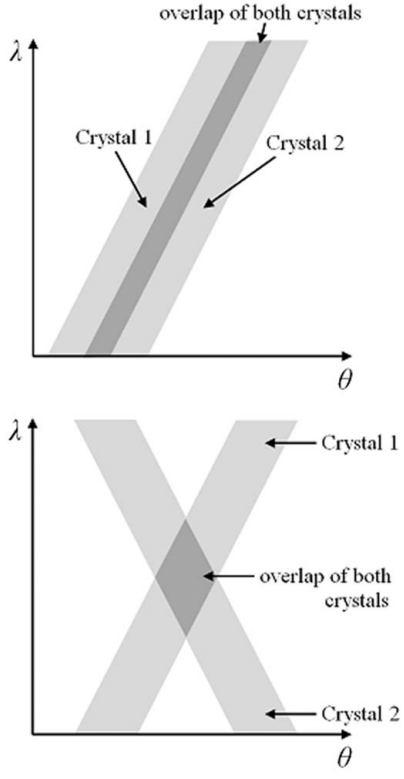

Figure 3
DuMond diagrams for two identical crystals arranged non-dispersively (top) and dispersively (bottom). Over small ranges of θ, the crystal traces may be treated as lines, as shown here. For the non-dispersive case, the trace of the second crystal is shown shifted against that of the first for clarity. The light grey regions show the wavelengths and incidence angles of the rays selected by either crystal. The dark grey region in each plot shows the wavelengths and incidence angles selected by both crystals.

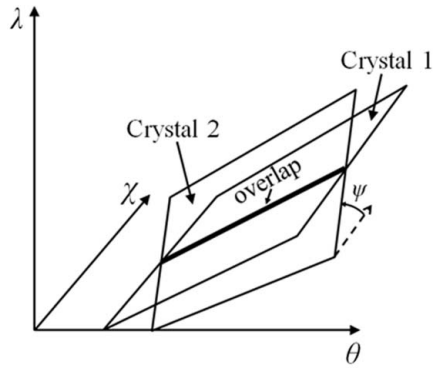

Figure 4
Expanded DuMond diagram for two identical crystals in which the second crystal is rotated by ψ about its incident beam with respect to the first. For ranges of χ under 1 mrad and small ranges of θ, the traces of the crystals may be treated as planes as shown here. The thick dark line shows the wavelengths, in-plane angles θ and out-of-plane angles χ that are selected by both crystals. For $\psi = 0^\circ$ and $\psi = 180^\circ$ this diagram yields, respectively, the non-dispersive and dispersive configurations shown in Fig. 2. Note that ψ in this figure is simply related to φ as defined in Fig. 1 and equations (1)–(4), $\psi = \varphi - 90^\circ$.

DCD are non-dispersively arranged at $\varphi = 90^\circ$ ($\psi = 0^\circ$ in Fig. 4), and would be dispersively arranged at $\varphi = 270^\circ$ ($\psi = 180^\circ$ in Fig. 4) if the DCD stages could rotate that far. The standard DuMond diagram does not cover arbitrary values of φ that are required to describe the DCD. However, such cases can be treated if one adds a third axis representing the out-of-plane ray angle, χ, to the standard DuMond diagram, making it three-dimensional. The three-dimensional DuMond diagram for the DCD can then be rotated about the θ-axis by the angle ψ, as shown in Fig. 4, to estimate the wavelengths and angles (θ, χ) that a ray must have to pass through both the monochromator and the DCD. If the incident beam divergence in either direction exceeds the Darwin widths of the crystals, then the total flux transmitted through the monochromator and DCD will depend strongly on φ. This dependence significantly outweighs the polarization dependence at the X-ray energies used here.

We have used *SHADOW* (Lai & Cerrina, 1986) to calculate the flux and polarization of the transmitted beam as a function of φ and energy (wavelength). These calculations used an established model of the beamline optics with a Gaussian source size (h × v) of 122.9 µm × 6.4 µm (r.m.s.) and a divergence of 24.2 µrad × 4.2 µrad (r.m.s.). In order to determine the best theoretical performance of the DCD, slope errors on the mirrors were neglected, and the alignment of all optical components of the beamline was assumed to be perfect. However, for mirror slope errors below 2 µrad (on I07 this has been shown experimentally to be the case) the loss of intensity to the sample is expected to be slight because the ray deflections remain below the Darwin widths of the crystals. The main influence of such slope errors is in the size of the achievable focal spot. Alignment errors are discussed in more detail below.

The total flux transmission calculated as a function of φ for four different energies is shown in Fig. 5. This shows the large variation in transmission even for a perfectly aligned system. This is mostly due to the narrow Darwin width of the silicon

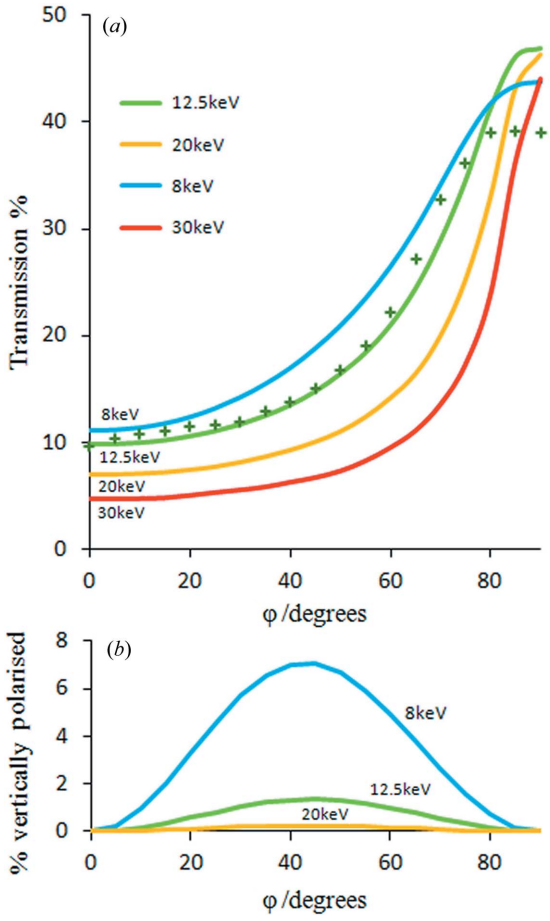

Figure 5
(*a*) Flux transmission as a function of φ for four different energies covering the full operational range, calculated assuming a Gaussian source distribution with no depth and completely horizontally polarized. The r.m.s. size was 122.9 µm × 6.4 µm and the r.m.s. divergence was 24.2 µrad × 4.2 µrad. The experimental data (crosses) have been arbitrarily scaled to match the theoretical prediction. (*b*) The proportion of the transmitted flux that is vertically polarized as a function of φ and energy.

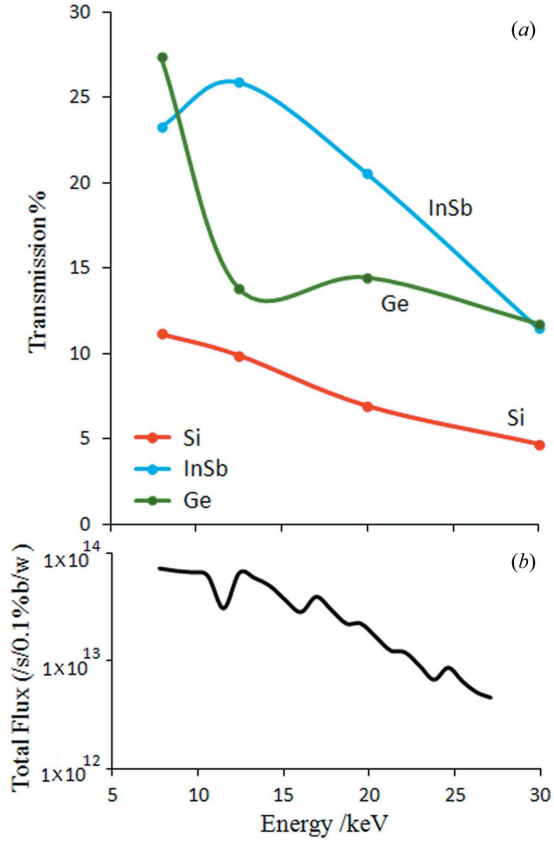

Figure 6
(*a*) The calculated flux transmission through the DCD as a function of energy at $\varphi = 0$. For silicon the transmission is only 5–10% whereas this can be significantly improved by replacing the DCD crystals. (*b*) Maximum flux before the DCD, at a ring current of 300 mA. Collimation and windows *etc.* can reduce this by up to half, which, for example, gives a flux at the sample position of $\sim 2 \times 10^{12}$ photons s^{-1} (0.1% bandwidth)$^{-1}$ (at 12.5 keV and $\varphi = 0$).

crystals compared with the divergence of the beam on I07. Since this width is also energy dependent [the width for Si(111) is ∼20 µrad at 12.5 keV and ∼9 µrad at 28 keV)], we additionally see a reduction in the transmission at higher energies. In addition, the source flux is also significantly lower at higher energies as can be seen in Fig. 6(*b*). The overall result is a considerably lower flux at higher energies. The form of these calculations compares well with the experimentally measured transmission through the DCD.

Fig. 5(*b*) shows how the proportion of the transmitted X-rays that are vertically polarized varies as a function of φ and energy. Even at 8 keV the contribution of vertically polarized X-rays is never more than 7% of the total flux (at $\varphi = \sim 45^\circ$), and at the typical operational angles for most reflectivity measurements on water ($0 \leq \varphi \leq 20$) it is less than ∼3%.

In order to improve the flux transmission we plan to replace the silicon crystals in the DCD with an alternative set of indium antimonide crystals. These crystals have a significantly broader Darwin width that is comparable with the horizontal beam divergence even at 30 keV. The result is a significant increase to the transmitted flux and this is shown in Fig. 6(*a*). For example, at 30 keV the flux transmitted through the DCD is improved by a factor of 2.5 at $Q_z = 0$ by using indium antimonide instead of silicon crystals. It is worth noting that we have rejected the possible alternative use of germanium crystals because their absorption *K*-edge occurs at the optimal energy of the DCD (the germanium *K*-edge is at 11.103 keV compared with the indium *K*-edge at 27.94 keV, the top end of the operational range). This significantly reduces the transmitted flux for germanium crystals relative to indium antimonide (see Fig. 6).

In principle, a change of the monochromator crystals would also improve the transmitted flux. However, indium antimonide is not suitable for use in the monochromator since its thermal conductivity is not adequate to dissipate the power load from the source, even when cryogenically cooled. There may, however, be some gain from using germanium in the monochromator. A horizontally scattering monochromator would also have a significant effect on the transmitted flux.

Of course, all of these calculations assume perfect alignment. However, although a number of lead counterweights are used to try to optimize the position of the centre of gravity of the system, it is inevitable that there is some parasitic 'wobble'

of the mechanics as the main circle is rotated. This wobble is enough to cause a parasitic change in the crystal pitches which is a significant proportion of the width of the rocking curves of the crystals. As a result there can be a fall off in the intensity if the pitch angles of the crystals are held constant during a scan of φ. The rate at which this occurs is dependent on the energy and is more significant at higher energies. Depending on the experimental requirements, the intensity can be recovered by making very small corrections to the crystal pitch, but in many cases this is unnecessary since the intensity variation is relatively small over the measurement range and can be compensated for by normalization.

2.2. Attenuation and collimation

The beamline attenuators are used to reduce the flux of the beam as required. These consist of eleven aluminium and molybdenum foils of various thicknesses that can intercept the beam upstream of the DCD. These are commonly used during a reflectivity measurement, with overlapping regions measured to allow for comparative normalization of the different parts of the curve.

There are two sets of slits between the mirrors and the DCD, which are used to improve the collimation of the beam entering the DCD with only a small loss of flux. These are principally for background reduction as the beam size is defined not by the collimation but by the focus point of the mirrors. The DCD crystals themselves also effectively act as a set of collimating slits since, as we discussed above, they select only a subset of the incoming beam within the Darwin width of the crystals. Post-DCD the space constraints and the need to track the moving beam mean that it is not presently possible to place a set of slits close to the sample. We are presently considering the possibilities for future inclusion of either some slits or a small aperture that can track the moving incident beam and could be used to reduce the beam size (and flux) at the sample position.

2.3. Incident beam monitoring

Internal to the vacuum vessel there is an incident beam monitor that is mounted on the diagnostics arm and moves with the DCD main rotation. This monitor detects the scattering from a kapton foil into an approximately perpendicular photodiode. This works reasonably well for a beam with no attenuation but is not sensitive enough to accurately measure the flux when the beam is attenuated.

Alternatively, subject to space constraints, an ion chamber can be placed outside of the vessel. The ion chamber does not move but has an aperture that is large enough to cover a limited range of beam deflection angles as it exits the DCD (usually acceptable for Q_z up to 1 Å^{-1} for most energies). There is a small change in the path length of the beam within the ion chamber but this has a negligible effect on the measured intensity.

Neither of these options are ideal and we anticipate including the possibility of an alternative set of attenuators positioned after the monitor as part of a the upgrade to include post-DCD slits.

2.4. Beam size and footprint variation at the sample position

The typical beam size at the sample position (measured normal to the beam axis) is $\sim$150 (v) $\times$ 200 (h) µm and is more or less independent of the incident angle. This large beam means that in some cases the beam footprint on a sample surface can be quite long. The footprint size at the critical edge of water is shown in Fig. 2 and may be problematic for some studies. As well as the post-DCD slits mentioned above, a possible future micro-focus upgrade is being considered to resolve this problem but in many cases the footprint can either be accommodated on a large trough or *via* the application of a geometrical correction to the data (Salah *et al.*, 2007), although care must be taken to account for the meniscus.

The beam also pivots at the sample position as the main circle is rotated. The variation of this angle, β, is also energy dependent, but over most Q-ranges of interest the variation is small ($<1.5^\circ$ variation of β for Q_z up to 1 Å^{-1}). Still, this variation does present some small restrictions to the sample environment. In principle there is also a minor geometrical contribution to a footprint correction, that is dependent on the relative size and shape of the liquid trough in use, but this is essentially negligible since the typical variation in footprint length is less than 0.0001% for the angles where the footprint is longer than the sample.

An additional effect of the footprint is important for wide-angle GIXD. The length of the footprint directly reduces the angular resolution and this effect is significantly more important at wide angles. Although a pair of slits or a set of soller slits can be used to define the angle, when using an area detector it is recommended to use a one-dimensional pinhole geometry (Meron *et al.*, 2009). In this case the resolution is defined by the combination of detector and slit distances and the size of the slit.

2.5. Detectors

The main detector used with the DCD is the Pilatus 100K mounted on the diffractometer detector arm (point detectors are also available). This detector can be positioned at a distance of $\sim$0.5–0.9 m from the sample (depending on sample environment constraints) and has an evacuated flight tube. A set of slits ($\sim$100–280 mm from the sample) can be used to reduce background for reflectivity measurements and/or importantly to allow the definition of a 'pinhole' for GIXD measurements (Meron *et al.*, 2009). The fact that this detector is mounted on the diffractometer means that it is very easy to change between specular and off-specular measurements.

Alternatively a Pilatus 2M detector can be used in combination with a long flight tube for GISAXS measurements requiring longer camera lengths than are achievable with the diffractometer mounted detectors. This detector is static during the reflectivity measurements; instead a region of interest moves on the detector to track the reflected beam.

The flight tube (He atmosphere) has an internal beam stop which can be positioned to block the direct and reflected beam to allow GISAXS measurements. The minimum camera length possible using this detector is ~1.5 m, while the maximum camera length is energy dependent (limited by space constraints owing to the horizontal deflection of the beam) and is shown in Fig. 2(*b*). The detector is mounted on a movable stage which can be positioned horizontally (up to 0.5 m from reflected beam) and vertically (up to 0.3 m from reflected beam) as required to cover a wide range of possible Q.

2.6. Errors

There are a number of contributions to the error in the momentum transfer calculated from the position of the main circle. The contributions to the errors include: the overall system alignment relative to the incoming beam and diffractometer, the parasitic motions as the circle is moved, the accuracy of the zero calibration, the beam divergence and the accuracy of the sample height alignment. It is difficult to precisely quantify these errors owing to the complexity of the system. However, the isolation of the detector arm from the DCD axes is both a means of checking the calculation and compensating for any errors. Since we know that the liquid surface is truly flat, we are sure that the angle of the reflected beam must be equal to the incidence angle. Thus, because we calculate the position of the detector based on the theoretical Q_z, any deviation from the calculated position is an indication of an error in either the sample height or the Q-calculation due to alignment errors. Owing to air and/or water diffuse scattering, the apparent beam size at the detector is usually larger than the detector pixel size of 172 µm, but it is possible to determine small movements of the beam on the detector. A move of one pixel corresponds to an error in Q_z of ~0.002 Å^{-1} at 12.5 keV, although with good alignment such a large movement is not practically seen.

The errors in alignment of the DCD itself are generally dwarfed by any error in the sample height alignment. If the height is incorrect then the beam will move on the sample surface and this can produce a relatively large movement of the beam at the detector. Because of this, frequent realignment between reflectivity scans may be required to account for evaporation. This is trivial and can easily be incorporated into repeated measurements or automated measurement scripts. With this consideration, and because use of the area detector means that we always collect the reflected beam, there is no loss of the measured intensity as a result of a small misalignment. Any error in the calculated Q_z can be measured as the deviation from the calculated position, while the full intensity of the beam is recorded.

3. Control and operation

The system is controlled through the in-house software *Generic Data Acquisition* (*GDA*).

Since several motors need to move for any given incidence angle from the DCD, *GDA* has some virtual motors that move all the appropriate axes (including the detector arm or region of interest within a detector) to the correct positions. Thus the incident angle can be simply set or scanned with a simple command. The only alignment required is a height scan which is also straightforward and can be done automatically. The use of regions of interest on the area detector means that both the signal and a background can be measured simultaneously, and, as mentioned above, provides a good indication of the accuracy of the alignment.

4. Examples of data from commissioning and early experiments

Reflectivity measurements from the DCD are reproducible and for air–water fit the theoretical curve very well. Fig. 7 shows the reflectivity of water measured at 12.5 and 20 keV. The data at 20 keV are almost indistinguishable from the lower-energy data, other than being noisier and quicker to reach the background, owing to the reduced flux at this energy. [For comparison a typical flux to be expected at 12.5 keV is ~2×10^{12} photons s^{-1} (0.1% bandwidth)$^{-1}$ and at 20 keV it is ~5×10^{11} photons s^{-1} (0.1% bandwidth)$^{-1}$.] Counting times

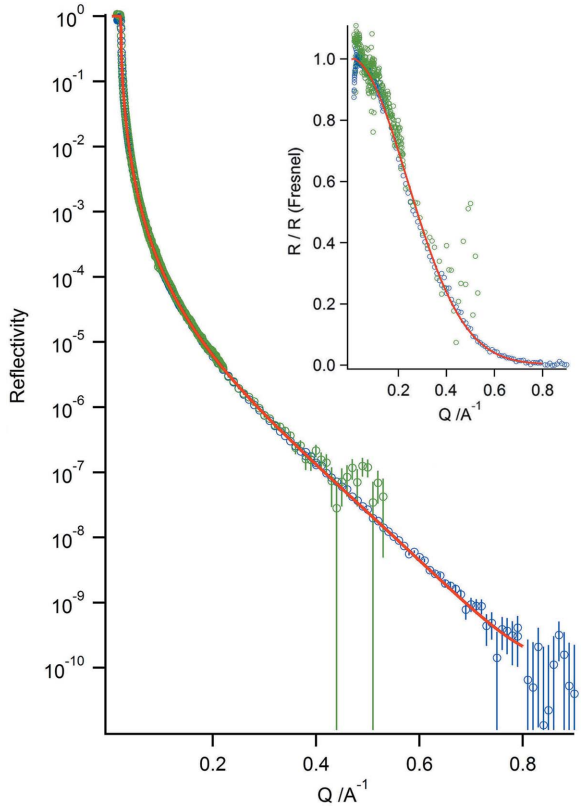

Figure 7
Fit (red) of reflectivity data from pure water measured at 12.5 keV (blue) and 20 keV (green). In both cases a background 'region of interest' has been subtracted (measured simultaneously). The inset shows the same data normalized to the Fresnel reflectivity. The fit parameters, background = 10^{-10} and roughness = 2.9 Å, were calculated using *Motofit* (Nelson, 2006).

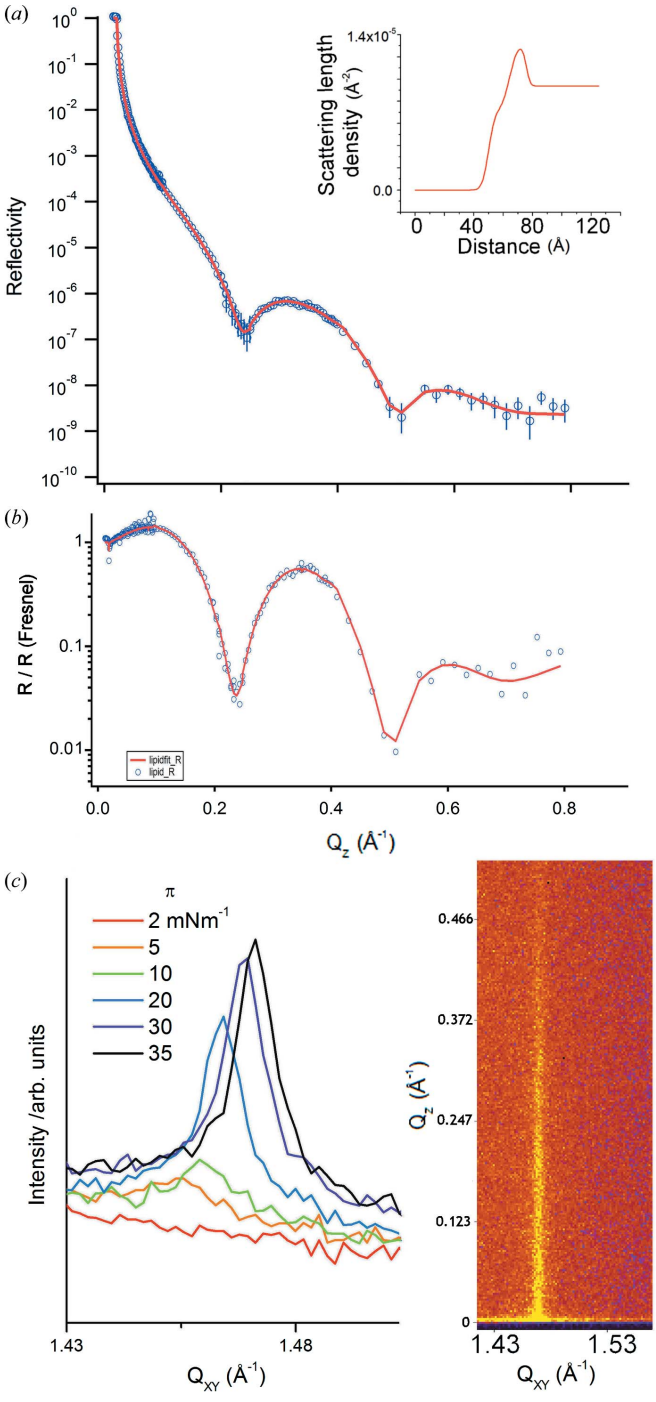

Figure 8
(*a*) An example of reflectivity (and corresponding fit) from a lipid layer (DPPC) on water containing 0.1 m*M* Ca^{2+} at a surface pressure of 30 mN m^{-1} (measured by Roser *et al.*, unpublished). (*b*) The same data normalized to the Fresnel reflectivity. (*c*) The variation of GIXD for DPPC as a function of surface pressures, π, together with an example Pilatus image (at 35 mN m^{-1}) collected using the pin-hole geometry (Meron *et al.*, 2009).

were the same for each data set (1 s per point) so the higher-energy data could be improved by counting for longer at high Q. The Q resolution is effected by many factors including the X-ray energy, the Darwin widths of the crystals and beam divergence as well as the intrinsic properties of the DCD mechanics and alignment. The real resolution is small and not a limiting factor in most cases (of the order of 0.0001 Å^{-1}).

An illustration of the combination of reflectivity and GIXD is given in the study of phospholipids at the air–water interface. Fig. 8 shows the fitted reflectivity from a typical layer of DPPC (dipalmitoylphosphatidylcholine) measured at 12.5 keV, together with corresponding GIXD data as a function of surface pressure. The GIXD data can be measured in 10–30 s but does show some beam damage effects. Incorporation of a fast shutter and helium atmosphere significantly mitigates this, though for the most part damage only occurs when the attenuation is minimal (and so is not a significant problem during the reflectivity measurement which, for the most part, is performed with high attenuation). Rastering across the surface is also straightforward, so multiple measurements of the same film in order to reduce exposure are trivial. At 12.5 keV a full set of reflectivity and GIXD can be measured in about 10–20 min depending on the required resolution.

5. Conclusion

The double-crystal deflector described here is fully functional and in routine operation on beamline I07. The standard energy used is 12.5 keV, but other energies (10–28 keV) are also available. A range of experiments have been performed successfully including combined reflectivity measurements with GIXD and time-resolved GISAXS. This transition between techniques is particularly straightforward and the resultant easy combination of techniques makes for a particularly powerful experimental tool. Although the system now works well and reproducibly, we are planning some upgrades to improve certain aspects, flux transmission at higher energies and beam size in particular.

A large number of people have contributed to the success of this development. In particular we would like to thank O. Konovalov, V. Honkimäki and H. Reichert for the original suggestion, explanation of the ID15 system and the initial discussions on the potential design; B. M. Murphy for her helpful discussion regarding the design of LISA; A. Warne, Y. Lifshitz, J. Emmins, X. Ren, E. Shepherd, H. Patel, S. Alcock, M. Harrall, M. Sussmuth and M. Matthews for their help during assembly and commissioning; and S. J. Roser, K. Edler, A. Zarbakhsh, J. W. White, J.-M. Lin and M. Schlossman for their considerable help during the design and/or commissioning of the system, and for use of data from their experiments. The internal optics of the DCD were assembled by ADC Inc.

References

Daillant, J. (2000). *Curr. Sci.* **78**, 1496–1506.
DuMond, J. W. M. (1937). *Phys. Rev.* **52**, 872–883.
Honkimäki, V., Reichert, H., Okasinski, J. S. & Dosch, H. (2006). *J. Synchrotron Rad.* **13**, 426–431.

Lai, B. & Cerrina, F. (1986). *Nucl. Instrum. Methods Phys. Res. A*, **246**, 337–341.
Meron, M., Gebhardt, J., Brewer, H., Viccaro, J. P. & Lin, B. (2009). *Eur. Phys. J. Special Topics*, **167**, 137–142.
Murphy, B. M., Greve, M., Runge, B., Koops, C. T., Elsen, A., Stettner, J., Seeck, O. H. & Magnussen, O. M. (2010). *ACS Conf. Proc.* **1234**, 155–158.
Nelson, A. (2006). *J. Appl. Cryst.* **39**, 273–276.
Salah, F., Harzallah, B. & van der Lee, A. (2007). *J. Appl. Cryst.* **40**, 813–819.
Schlossman, M. L., Synal, D., Guan, Y., Meron, M., Shea-McCarthy, G., Huang, Z., Acero, A., Williams, S. M., Rice, S. A. & Viccaro, P. J. (1997). *Rev. Sci. Instrum.* **68**, 4372–4384.
Seeck, O. H., Deiter, C., Pflaum, K., Bertam, F., Beerlink, A., Franz, H., Horbach, J., Schulte-Schrepping, H., Murphy, B. M., Greve, M. & Magnussen, O. (2012). *J. Synchrotron Rad.* **19**, 30–38.
Smilgies, D.-M., Boudet, N., Struth, B. & Konovalov, O. (2005). *J. Synchrotron Rad.* **12**, 329–339.
Zachariasen, W. H. (1945). *Theory of X-ray Diffraction in Crystals.* New York: John Wiley and Sons.